Nonequilibrium Green's Function Modeling of type-II Superlattice Detectors and its Connection to Semiclassical Approaches

Francesco Bertazzi,[1,2,*] Alberto Tibaldi,[1,2,†] Michele Goano,[1,2] Jesus Alberto Gonzalez Montoya,[1] and Enrico Bellotti[3]

[1] *DET, Politecnico di Torino, Torino, Italy*
[2] *IEIIT-CNR, Torino, Italy*
[3] *ECE Department, Boston University, Boston, Massachusetts, USA*

(Received 27 April 2020; revised 22 June 2020; accepted 29 June 2020; published 28 July 2020)

Theoretical investigations of carrier transport in type-II superlattice detectors have been mostly limited to simplified semiclassical treatments, due to the computational challenges posed by quantum kinetic approaches. For example, interband tunneling in broken-gap configurations calls for a multiband description of the electronic structure, and spatially indirect optical transitions in superlattice absorbers require fully nonlocal carrier-photon self-energies. Moreover, a large number of iterations is needed to achieve self-consistency between Green's functions and self-energies in the presence of strongly localized states not directly accessible from the contacts. We demonstrate an accurate, yet computationally feasible nonequilibrium Green's function model of superlattice detectors by formulating the kinetic equations in terms of problem-matched maximally localized basis functions, numerically generated from few modes representing the main conductive channels of the nanostructure. The contribution of all the remaining modes is folded in an additional self-energy to ensure current conservation. Inspection of spatially and energetically resolved single particle properties offers insight into the complex nature of carrier transport in type-II superlattice detectors, and the connection to semiclassical approaches enables the interpretation of mobility experiments.

DOI: 10.1103/PhysRevApplied.14.014083

I. INTRODUCTION

The nearly lattice-matched 6.1 Å semiconductor family, which includes GaSb, AlSb, InAs, and their related compounds, offers a viable alternative to the state-of-the-art infrared imaging technology based on bulk (Hg, Cd)Te; see Ref. [1] for a comparative study. The tunability of the detection wavelength over most of the technologically relevant infrared spectrum, the possibility of even realizing different energy-band alignments, from type-I to type-II broken-gap (misaligned, or type-III) superlattices, and the band structure flexibility in controlling conduction and valence band edges independently through adjustment of the constituent layer compositions and/or thicknesses have led to the development of new device concepts and architectures with potentially suppressed Auger generation rates, lower dark currents, and, consequently, higher operating temperature [1]. Whether this technology will reach its potential depends on technological parameters such as Shockley-Read-Hall (SRH) lifetimes, but also on the understanding of the underlying physics. Theoretical investigations based on simple band-structure arguments have not been conclusive, probably because carrier transport in type-II superlattices (T2SLs) is not quite fitting a single picture, but rather involves the combination and possibly the transition between different mechanisms, from miniband (coherent) transport to (incoherent) sequential tunneling, or even Wannier-Stark hopping, depending on built-in and/or applied fields. A self-consistent description of carrier transport and optical absorption in T2SLs can be obtained by a quantum-kinetic framework based on a nonequilibrium Green's function (NEGF) approach. The present implementation includes acoustic scattering in the equipartition approximation, inelastic polar optical scattering, and carrier-photon scattering [2–4], described by fully nonlocal self-energies computed in the self-consistent Born approximation (SCBA) [5].

The electronic structure of T2SLs has been described using a variety of theoretical approaches, such as the empirical tight-binding method [6], the empirical pseudopotential method [7], and multiband $k \cdot p$ models

*francesco.bertazzi@polito.it
†alberto.tibaldi@polito.it

within the envelope function approximation [8–10]. With the inclusion of the first conduction band, heavy-hole, light-hole, and spin-orbit split-off bands, the multiband 8×8 $k \cdot p$ model seems a good compromise between accuracy and computational efficiency. The nonlocality of the carrier-photon interaction, the slow convergence of the self-consistent calculation of Green's functions and self-energies in the presence of strong confinement [11], and the large number of unknowns needed for spatial resolution in realistic devices can easily lead to a staggering computational effort. Moving to a mode-space basis [12,13] is particularly advantageous in the analysis of *supercell* superlattice detectors, such as graded-gap M- and W-structures, complementary barrier detectors with superlattice absorbers surrounded by electron- and hole-blocking unipolar barriers, and interband cascade IR photodetectors, in which the transport of the photogenerated carriers is mediated by few discrete states, possibly forming a miniband, rather than through the coupling to the continuum spectrum of the bulk layers embedding the active region of *buried* junction detectors [14].

II. THEORY

Consider a system evolving under the Hamiltonian operator

$$\hat{\mathcal{H}} = \hat{H} + \hat{H}_{ep} + \hat{H}_{e\gamma}, \tag{1}$$

where $\hat{H}$ is the exactly solvable part of the superlattice Hamiltonian that contains the lattice and the electrostatic potential, and $\hat{H}_{ep}$ and $\hat{H}_{e\gamma}$ are the many-body components that include carrier-phonon and carrier-photon interactions, respectively. Carrier-carrier interactions are included at the Hartree level through coupling to Poisson's equation. Electron-electron interactions beyond the mean-field approximation may be considered by explicit inclusion of dynamical screening through the *GW* formalism [15,16]. In general, electron-electron scattering may change the intraband carrier dynamics by setting up a heated Maxwellian distribution, redistributing the electron population between subbands [17]. For example, in hot-carrier solar cells, electron-electron scattering is responsible for the fast photocarrier escape from the confined absorber states to the extended quasicontinuum states via thermionic emission [16]. The effect was observed at high incident optical power densities, corresponding to photon fluxes greater than 10^{19} photons/cm^2/s [18]. Since IR detectors operate at low injection levels, with photon fluxes below 10^{14} photons/cm^2/s in the long-wavelength infrared (LWIR) spectral range (the final photon flux incident on the IR detector depends on many quantities, including temperature of the target and spectral black body curve, spectral band and accompanying atmospheric transmission, f number of the objective, and transmission through the optics) [19], we do not expect electron-electron scattering to play a significant role. As for the optical properties, the excitonic enhancement of interband transitions (electron-hole interaction) is also negligible, since the excitonic binding energy is small (approximately 2 meV) [9].

A. Real-space analysis

The starting point is the eight-band Pidgeon-Brown or Enders's $k \cdot p$ Hamiltonian [20]

$$H_{k\cdot p}(\underline{K}) = \begin{bmatrix}
E_g + A_c(k_x^2+k_y^2+k_z^2) & iPk_x & iPk_y & iPk_z \\
-iPk_x & Lk_x^2 + M(k_y^2+k_z^2) - \Delta/3 & Nk_xk_y - i\Delta/3 & k_xN_+k_z + k_zN_-k_x \\
-iPk_y & Nk_xk_y + i\Delta/3 & Lk_y^2 + M(k_x^2+k_z^2) - \Delta/3 & k_yN_+k_z + k_zN_-k_y \\
-iPk_z & k_zN_+k_x + k_xN_-k_z & k_zN_+k_y + k_yN_-k_z & Lk_z^2 + M(k_x^2+k_y^2) - \Delta/3 \\
0 & 0 & 0 & 0 \\
0 & 0 & 0 & -\Delta/3 \\
0 & 0 & 0 & -i\Delta/3 \\
0 & \Delta/3 & i\Delta/3 & 0
\end{bmatrix}$$

$$\begin{bmatrix}
0 & 0 & 0 & 0 \\
0 & 0 & 0 & \Delta/3 \\
0 & 0 & 0 & -i\Delta/3 \\
0 & -\Delta/3 & i\Delta/3 & 0 \\
E_g + A_c(k_x^2+k_y^2+k_z^2) & iPk_x & iPk_y & iPk_z \\
-iPk_x & Lk_x^2 + M(k_y^2+k_z^2) - \Delta/3 & Nk_xk_y + i\Delta/3 & k_xN_+k_z + k_zN_-k_x \\
-iPk_y & Nk_xk_y - i\Delta/3 & Lk_y^2 + M(k_x^2+k_z^2) - \Delta/3 & k_yN_+k_z + k_zN_-k_y \\
-iPk_z & k_zN_+k_x + k_xN_-k_z & k_zN_+k_y + k_yN_-k_z & Lk_z^2 + M(k_x^2+k_y^2) - \Delta/3
\end{bmatrix}, \tag{2}$$

written in the zone-center basis

$$S\uparrow, X\uparrow, Y\uparrow, Z\uparrow, S\downarrow, X\downarrow, Y\downarrow, Z\downarrow, \tag{3}$$

where $\underline{K} = (k_x, k_y, k_z)$ (in the following, upper-case letters are for three-dimensional wavevectors and positions), E_g is the fundamental gap of the unstrained material, Δ

is the spin-orbit splitting, P is the interband momentum matrix element, and the renormalized parameters A_c, L, M, and N are obtained from the conduction band effective mass m_c^* and the modified Luttinger parameters in which the remote contribution of the conduction band has been subtracted [21]:

$$A_c = \frac{\hbar^2}{2m_c^*} - \frac{2P^2}{3E_g} - \frac{P^2}{3(E_g+\Delta)}, \tag{4}$$

$$L = -\frac{\hbar^2}{2m_0}(\gamma_1 + 4\gamma_2), \tag{5}$$

$$M = -\frac{\hbar^2}{2m_0}(\gamma_1 - 2\gamma_2), \tag{6}$$

$$N = -\frac{\hbar^2}{2m_0}6\gamma_3. \tag{7}$$

In principle, $k\cdot p$ parameters can be derived from full-Brillouin-zone band structure calculations [22], but here we adopt the semiempirical parameter set reported in Refs. [9,10], with band offsets and bowing parameters from Ref. [23]. InAs and GaSb are almost lattice matched, while InAs/(In, As)Sb SLs require strain-balancing techniques [24]. Strain is included in the $k\cdot p$ Hamiltonian (2) as described in Ref. [20]. In the atomic basis (3), the spin-orbit part of the Hamiltonian is nondiagonal, but Burt-Foreman operator ordering can be more easily defined [21,25]. According to operator ordering, the Kane parameter N is split into two asymmetric parts, $N = N_+ + N_-$ with $N_- = M - \hbar^2/(2m_0)$. The splitting is shown only for the matrix elements of Eq. (2) that are linear in k_z, assuming that z is the only symmetry-broken direction. Moving to the atomiclike basis set defined in Refs. [26,27], within the axial approximation, the bulk Hamiltonian block diagonalizes with respect to the spin components, i.e., the 8×8 Hamiltonian decouples into two 4×4 blocks, and the energy dispersion becomes isotropic in the transverse wavevector, which simplifies the numerical integration of the self-energies. Rewriting the bulk $k\cdot p$ Hamiltonian as [28]

$$H_{k\cdot p}(\underline{K}) = H_2(\underline{k})k_z^2 + H_1(\underline{k})k_z + H_0(\underline{k}), \tag{8}$$

where $\underline{k}$ is the transverse component of $\underline{K}$, and replacing k_z with the corresponding operator $-i\partial_z$, gives the differential Hamiltonian operator

$$H_{k\cdot p}(\underline{k},z) = -\partial_z H_2(\underline{k},z)\partial_z + H_{1L}(\underline{k},z)\partial_z + \partial_z H_{1R}(\underline{k},z) + H_0(\underline{k},z). \tag{9}$$

In the envelope function approximation, the nanostructure wavefunction includes a plane wave in the transverse direction, the zone-center Bloch functions $u_a(\underline{R})$ listed in Eq. (3), and the slowly varying envelopes $\zeta_{\underline{k}\alpha}(z)$ that describe how the lattice-periodic functions are mixed together at every position in the symmetry-broken direction z:

$$\psi_{\underline{k}\alpha}(\underline{R}) = \frac{1}{\sqrt{A}} e^{i\underline{k}\cdot\underline{r}} u_a(\underline{R})\zeta_{\underline{k}\alpha}(z). \tag{10}$$

Here $\underline{r}$ represents the translational invariant directions (x,y), $\underline{R} = (\underline{r},z)$, $\alpha = (a,i)$ is a compound index combining indices a for band and i for space, and A is the normalization area. Expanding the envelope functions in first-order Lagrange polynomials, the finite-element procedure gives the steady-state Dyson and Keldysh equations in full matrix notation [2,3,29]

$$[EM - H(\underline{k}) - \Sigma^R(\underline{k},E)]G^R(\underline{k},E) = I, \tag{11a}$$

$$G^{\lessgtr}(\underline{k},E) = G^R(\underline{k},E)\Sigma^{\lessgtr}(\underline{k},E)G^A(\underline{k},E), \tag{11b}$$

in which a contravariant representation is used for Green's functions and a covariant representation for self-energies, with the two representations being related by the overlap matrix M. The self-energy $\Sigma = \Sigma^B + \Sigma^{e\gamma} + \Sigma^{ep}$ includes both the boundary and the scattering self-energies [3]. The boundary self-energies $\Sigma_B^{R\lessgtr}$ reflecting the openness of the system are obtained from the complex band structure of the reservoirs [30].

The vibrational properties of antimonide-based SLs are quite complex and still almost unexplored. The InAs/GaSb system has the broken-gap type-II electronic band alignment and overlapping optical phonon spectra of the two constituents [31,32], while the InAs/(In, As)Sb SLs system has staggered type-II electronic band alignment and staggered overlapping optical phonon spectra [33], which produces in both cases a wealth of possible phonon modes, including bulklike (confined in one of the two constituents or extended in both) and interface phonon modes. The interaction with bulklike modes is usually reduced in short-period SLs, but this reduction is balanced by the increasing contribution of interface modes [34], whose properties critically depend on technological details, such as interfacial bonding, compositional modulation, and alloy disorder [35]. Considering the uncertainties in the phonon spectra (as-grown SLs may significantly differ from design intentions) [35], we assume that the electrons interact with bulk phonon modes. We will revisit this approximation in a future work. Coupling to acoustic and polar optical phonons is considered within the deformation potential and the Fröhlich formalism, respectively, by means of fully nonlocal self-energies $\Sigma_{ep}^{R\lessgtr}$ computed in the self-consistent

Born approximation [2]

$$[\Sigma^{\lessgtr}_{ep}(\underline{k},E)]_{\alpha\beta} = \sum_{\underline{Q}} |U_{\underline{Q}}|^2 e^{iq_z(z_i-z_j)} \times \{M[N_{\underline{Q}} G^{\lessgtr}(\underline{k}-\underline{q},E\mp\hbar\omega_{\underline{Q}}) + (N_{\underline{Q}}+1)G^{\lessgtr}(\underline{k}-\underline{q},E\pm\hbar\omega_{\underline{Q}})]M\}_{\alpha\beta}, \tag{12}$$

where $\alpha = (a,i)$ and $\beta = (b,j)$. Phonon occupation numbers $N_{\underline{Q}}$ in the (three-dimensional) phonon wavevectors $\underline{Q} = (q,q_z)$ are computed according to Bose-Einstein statistics. Hot phonon effects are negligible, since background doping and photogenerated carrier concentrations in IR SL absorbers are too small to drive the phonon population out of equilibrium by polar optical emission [36]. Neglecting the principal part, which just leads to energy renormalization, the retarded component of the self-energy reads [37]

$$[\Sigma^{R}_{ep}(\underline{k},E)]_{\alpha\beta} = \sum_{\underline{Q}} |U_{\underline{Q}}|^2 e^{iq_z(z_i-z_j)} \times \{M[N_{\underline{Q}}\, G^{R}(\underline{k}-\underline{q},E+\hbar\omega_{\underline{Q}}) + (N_{\underline{Q}}+1)G^{R}(\underline{k}-\underline{q},E-\hbar\omega_{\underline{Q}}) + \tfrac{1}{2}G^{<}(\underline{k}-\underline{q},E-\hbar\omega_{\underline{Q}}) - \tfrac{1}{2}G^{<}(\underline{k}-\underline{q},E+\hbar\omega_{\underline{Q}})]M\}_{\alpha\beta}. \tag{13}$$

According to deformation-potential scattering theory, the scattering strength $U_{\underline{Q}}$ due to the interaction with acoustic modes is described by

$$U_{\underline{Q}} = \sqrt{\frac{\hbar D_a^2}{2V\rho u_l}Q}, \tag{14}$$

where u_l is the longitudinal sound velocity in the material, $D_a = 8$ eV is the deformation potential [[38], Chapter 5], ρ is the semiconductor mass density, and V is the normalization volume. Unless specified, material parameters are from Ref. [39]. Assuming a dispersion-less longitudinal optical phonon with energy $\hbar\omega_{\mathrm{LO}} = 30$ meV, Fröhlich theory of polar optical scattering gives the interaction strength

$$U_{\underline{Q}} = \sqrt{\frac{e^2\hbar\omega_{\mathrm{LO}}}{2V}\left(\frac{1}{\epsilon_\infty}-\frac{1}{\epsilon_s}\right)}\frac{Q}{Q^2+q_0^2}, \tag{15}$$

where ϵ_s and ϵ_∞ are the static and optical dielectric constants of the material, and q_0 is the inverse of the Debye-Hückel screening length (10 nm in all the simulations below). The electron-photon self-energy components read in full matrix notation [37,40,41]

$$\Sigma^{\lessgtr}_{e\gamma}(\underline{k},E) = \sum_{\lambda\underline{Q}} M^{\gamma}(\underline{k},\lambda)[N_{\lambda\underline{Q}}G^{\lessgtr}(\underline{k},E\mp\hbar\omega_{\lambda\underline{Q}}) + (N_{\lambda\underline{Q}}+1)G^{\lessgtr}(\underline{k},E\pm\hbar\omega_{\lambda\underline{Q}})]M^{\gamma}(\underline{k},\lambda), \tag{16a}$$

$$\Sigma^{R}_{e\gamma}(\underline{k},E) = \sum_{\lambda\underline{Q}} M^{\gamma}(\underline{k},\lambda)[N_{\lambda\underline{Q}}G^{R}(\underline{k},E+\hbar\omega_{\lambda\underline{Q}}) + (N_{\lambda\underline{Q}}+1)G^{R}(\underline{k},E-\hbar\omega_{\lambda\underline{Q}}) + \tfrac{1}{2}G^{<}(\underline{k},E-\hbar\omega_{\lambda\underline{Q}}) - \tfrac{1}{2}G^{<}(\underline{k},E+\hbar\omega_{\lambda\underline{Q}})]M^{\gamma}(\underline{k},\lambda), \tag{16b}$$

with

$$M^{\gamma}_{\alpha\beta}(\underline{k},\lambda) = \frac{e}{m_0}\sqrt{\frac{\hbar}{2\epsilon_0 V\omega_\gamma}}[\underline{\epsilon}_{\lambda\underline{Q}}\cdot\underline{p}_{\alpha\beta}(\underline{k})], \tag{17}$$

where $\underline{\epsilon}_{\lambda\underline{Q}}$ is the light polarization of the photon in mode λ and wavevector $\underline{Q}$, and the interband momentum matrix element is [42]

$$\underline{p}_{\alpha\beta}(\underline{k}) = \frac{m_0}{\hbar}\nabla_{\underline{K}}H_{\alpha\beta}(\underline{K}). \tag{18}$$

For a monochromatic illumination of energy $\hbar\omega_\gamma$ and light intensity J_γ, we replace $N_{\lambda\underline{Q}}$ with the number of photons $N_\gamma = \phi_{\omega_\gamma}V/\tilde{c}$, corresponding to the incoming flux $\phi_{\omega_\gamma} = J_\gamma/(\hbar\omega_\gamma)$ of photons with energy $\hbar\omega_\gamma$ and velocity $\tilde{c}$.

B. Mode-space analysis

Inspired by the spectral decomposition of Green's function [43], the main idea behind mode-space approaches is to transform the kinetic equations from the original real-space basis to a more convenient one defined by few basis functions, which should be as close as possible to the eigenstates of the nanostructure. A possible set of problem-matched basis functions can be obtained by selecting the eigenstates of the noninteracting Hamiltonian $\hat{H}_0$ (i.e., without boundary and scattering self-energies) with energies in a given energy range, representing all the relevant conduction channels of the nanodevice. In this representation, the number of basis functions required for a given accuracy should be much less than in the original space, reducing the computational effort significantly. Reduced-order models are usually limited to the coherent limit, since the extension to the dissipative case requires the scattering self-energies to be computed directly in the reduced subspace. An efficient implementation of scattering in mode space is based on the use of localized basis

functions obtained by diagonalizing the position operator in the new representation [44]. For field-periodic structures, e.g., quantum cascade lasers, this procedure leads to the definition of maximally localized Wannier functions [45,46]. Since every localized basis function is associated with the corresponding eigenposition, the scattering self-energies can be discretized directly in mode space, by just replacing the node coordinates of the mesh with these eigenpositions. The effectiveness of any mode-space approach obviously depends on the number of basis functions needed to accurately represent the self-energies, but a simple projection scheme violates current conservation, even in the coherent limit, due to the incomplete representation of the boundary self-energies [44].

In order to reduce the number of basis functions while still satisfying conservation rules, we propose a partitioning technique in which the eigenstates of the nanostructure are divided into two sets, a *near* set including the selected basis functions, and a *remote* set including all the other eigenstates. Current conservation is recovered by folding the influence of the remote modes in an additional self-energy, which is equivalent to the Hamiltonian-folding procedure commonly employed in real space to include the influence of the semi-infinite contacts without actually including them in the simulation domain [4]. More in detail, the numerical generation of problem-matched basis functions proceeds as follows. The generalized eigenvalue problem

$$H_0\psi_i = E_i M\psi_i \tag{19}$$

formulated in a finite-element overlapping basis is transformed by means of Löwdin symmetric orthogonalization to a standard eigenvalue problem with symmetrically orthogonalized functions, closest in the least square sense to the original nonorthogonal functions, thus eliminating the need for different contravariant and covariant representations for Green's functions and self-energies

$$M^{-1/2}H_0M^{-1/2}\psi_i = E_i\psi_i. \tag{20}$$

The solutions of Eq. (20) are classified as near or remote according to the proximity of their respective eigenvalue E_i to some value E_0 lying in the middle of the energy range considered. The position operator is then diagonalized in the near and remote representations to obtain maximally localized basis functions

$$\tilde{Z}_{\alpha_i}\psi^{\mathrm{ML}}_{\alpha_i} = z_{\alpha_i}\psi^{\mathrm{ML}}_{\alpha_i}, \tag{21}$$

with $\tilde{Z}_\alpha = T^\dagger_\alpha M^{-1/2}ZM^{-1/2}T_\alpha$, where Z is the finite-element representation of the position operator, and $T_\alpha = \{\psi_{\alpha_i}\}_{i=1}^{n_\alpha}$ is the transformation matrix whose columns are the near ($\alpha = n$) or remote ($\alpha = r$) modes. Having defined the transformation matrix $P = \{P_n, P_r\}$, with $P_\alpha = \{\psi^{ML}_{\alpha_i}\}_{i=1}^{n_\alpha}$, the Dyson and Keldysh equations for retarded and lesser components read in the complete (near plus remote) space

$$[\tilde{A}(\underline{k}) - \tilde{\Sigma}^R(\underline{k},E)]\tilde{G}^R(\underline{k},E) = I, \tag{22a}$$

$$\tilde{G}^<(\underline{k},E) = \tilde{G}^R(\underline{k},E)\tilde{\Sigma}^<(\underline{k},E)\tilde{G}^A(\underline{k},E), \tag{22b}$$

where $\tilde{A} = EI - \tilde{H}$, and Green's functions and self-energies are given by

$$\tilde{\Sigma} = P^\dagger T^\dagger M^{-1/2}\Sigma M^{-1/2}TP, \tag{23a}$$

$$\tilde{G} = P^\dagger T^\dagger M^{1/2}GM^{1/2}TP. \tag{23b}$$

Folding the influence of the remote states, the final form of the kinetic equations reads in block matrix notation

$$[\tilde{A}_{nn} - \tilde{\Sigma}^R_{nn} - \hat{\Sigma}^R_{nn}]\tilde{G}^R_{nn} = I_{nn}, \tag{24a}$$

$$\tilde{G}^<_{nn} = \tilde{G}^R_{nn}[\tilde{\Sigma}^<_{nn} + \hat{\Sigma}^<_{nn}]\tilde{G}^A_{nn}, \tag{24b}$$

in which we have defined an additional self-energy $\hat{\Sigma}$ representing the contribution of the remote modes to the coherent solution (the parametric dependence on the transverse wavevector and energy has been dropped for clarity):

$$\hat{\Sigma}^R_{nn} = \tilde{A}_{nr}\tilde{g}^R_{rr}\tilde{A}_{rn}, \tag{25a}$$

$$\hat{\Sigma}^<_{nn} = -\tilde{\Sigma}^{B<}_{nr}\tilde{g}^A_{rr}\tilde{A}^*_{rn} - \tilde{A}_{nr}\tilde{g}^R_{rr}\tilde{\Sigma}^{B<}_{rn} + \tilde{A}_{nr}\tilde{g}^<_{rr}\tilde{A}^*_{rn}. \tag{25b}$$

Here $\tilde{g}^R_{rr} = \tilde{A}^{-1}_{rr}$ and $\tilde{g}^<_{rr} = \tilde{g}^R_{rr}\,\tilde{\Sigma}^{B<}_{rr}\tilde{g}^A_{rr}$. From this point forward, the NEGF algorithm proceeds as usual, with the scattering self-energies computed directly in mode space, i.e., we replace in Eqs. (12) and (13) node coordinates with the eigenpositions z_{n_i} [44]. Once self-consistency is achieved between Green's functions and self-energies, the scattering self-energies are transformed back to real space, and the Dyson and Keldysh equations are solved in real space to obtain the relevant one-particle properties.

The self-consistent solution of Eq. (24) may take a large number of iterations to converge in the presence of strongly localized states outside the spectral supports of the contacts [11]. This limitation is not related to the mode-space representation, but it is intrinsic to the SCBA algorithm, which includes higher-order diagrams at each iteration, regardless of whether they are current conserving or not [47]. In fact, the slow convergence of the SCBA inspired the concept of the lowest-order approximation (LOA), which is based on the idea of collecting only

current-conserving diagrams at each scattering order. Several analytic continuation techniques were applied to the LOA series in order to reconstruct physical observables, proving that current conserving self-energies are not necessarily obtained through a self-consistent scheme [48–52]. These alternative approaches to the SCBA are compatible with mode-space approaches, but they will not be treated here.

In addition to convergence issues, the SCBA is formally valid only in the weak coupling limit. Because of the computational complexity of Hedin's equations for the inclusion of vertex corrections [53], the validity of the SCBA is seldom, if ever, discussed. One notable exception is a NEGF study of inelastic electronic transport in molecular devices, in which, depending on the initial conditions, the SCBA was shown to give multiple self-consistent solutions beyond a critical coupling electron-phonon strength [54]. Part of the reason why it is difficult to assess the limitations of the SCBA is that the numerical instabilities disappear if the Hartree part of the electron-phonon self-energy is neglected, as in most NEGF studies (including this work) of carrier transport in semiconductor nanostructures. The applicability of Fermi's golden rule to III nitrides despite their strong electron-phonon coupling [55] makes us confident in the validity of the SCBA in T2SLs, even in the presence of nearly dispersionless holes in the growth direction, due to the weakly ionic nature of the 6.1 Å material system and the strong anisotropy of the hole electronic structure [56,57].

III. RESULTS

The accuracy of the proposed approach and its applicability to complex T2SL-based architectures is discussed in Sec. III A. Interband cascade IR photodetectors (ICIPs) achieve high-temperature and high-speed operation by employing a discrete absorber architecture, each single absorber interposed between quantum-engineered electron and hole barriers to form a series of interband cascade stages. At high temperatures, the diffusion length is typically shorter than the absorption depth of the IR radiation. While the total thickness of the cascade can be comparable or even longer than the diffusion length, the photogenerated electrons travel only over one stage, which is significantly shorter than the diffusion length, before they recombine with the holes in the next stage. The structure considered here includes enhanced barriers, designed to suppress intraband-tunneling current between stages, and p-doped type-II InAs/GaSb superlattice absorbers [58]. Encompassing all the possible carrier transport mechanisms, including interband tunneling, ICIPs represent a good candidate for the accuracy assessment of the proposed mode-space approach. In Sec. III B we focus on the nature of carrier transport in LWIR SLs, and on the role of disorder. The connection to semiclassical approaches is made for the $InAs_{0.97}Sb_{0.03}/InAs_{0.55}Sb_{0.45}$ SL investigated experimentally in Ref. [59].

A. Accuracy assessment: ICIPs

In Fig. 1 we show the local density of states of the ICIP under consideration. The hole and electron barriers also serve as electron-relaxation and interband-tunneling regions, respectively. The electron-relaxation region is designed to facilitate the transport of photogenerated carriers from the conduction miniband of one stage to the valence miniband of the next [60]. For simplicity, the structure is considered in flat-band conditions, as the inclusion of space-charge effects will not affect the assessment of the proposed approach [61].

In Fig. 2(a) we show the spectral photocurrent in one stage of an ICIP illuminated by monochromatic light. In the original real-space representation, the device is discretized with a grid spacing of 0.5 nm, resulting, within our multiband $k \cdot p$ framework, in $n_t = 1160$ finite-element basis functions, while mode-space calculations are performed with $n_n = 250$ maximally localized basis functions, i.e., the matrix rank is reduced to approximately 22% of the original space. The continuous stripes in the current spectrum in the absorber region are indicative of miniband transport of the photogenerated electrons mediated by the extended states of the superlattice, while the staircase behavior in the relaxation layer is the signature of sequential tunneling. The interband tunneling through the

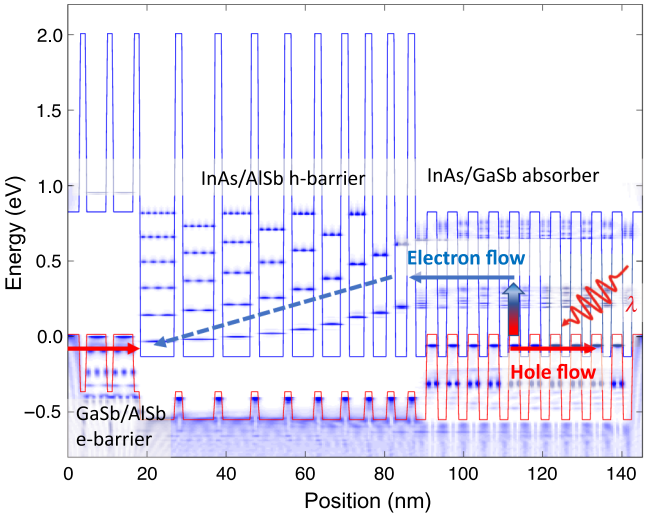

FIG. 1. Local density of states of one stage of a midwavelength infrared interband cascade photodetector shown for $\underline{k} = 0$ (color maps). The arrows indicate the direction of the electron and hole flows: the electron-hole pairs photogenerated in the superlattice absorber diffuse along the respective minibands, the electrons towards the hole barrier, where they relax by polar optical transitions down a Wannier-Stark ladder, until they reach the electron barrier, whereupon they tunnel into the valence miniband of the adjacent stage.

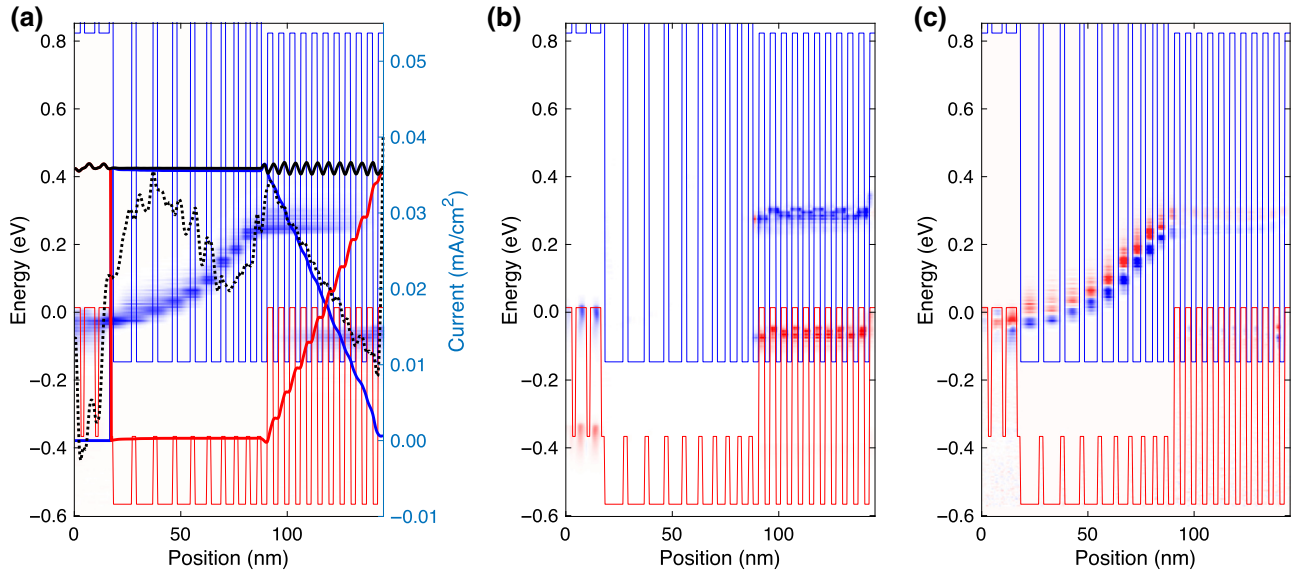

FIG. 2. (a) Spatially resolved photocurrent spectrum under a monochromatic illumination of 1 W/m^2 with $E_\gamma = 0.3$ eV (color maps). The corresponding energy-integrated current (black solid line, right axis) is approximately conserved, save for small oscillations due to the incompleteness of the basis set. Blue and red lines indicate electron and hole contributions, respectively. A position-dependent energy threshold is defined according to the local density of states to separate electron and hole contributions (solid blue and red lines, respectively). Current conservation is clearly violated if the contribution of the remote modes is neglected (black dotted line). (b) Spatially resolved radiative generation spectrum (color maps). (c) Spectral scattering current due to coupling to polar optical phonons [53], showing the relaxation of the carriers [positive (negative) values, i.e., in (out) scattering of electrons, have a gradient from white to blue (red)].

type-II broken gap and finally the recombination with the holes of the next stage is also clearly visible. Upon convergence, the total energy-integrated current (black solid line) is approximately conserved over the whole device region, which is a very stringent test for any NEGF model. Residual fluctuations in the coherent current shown in Fig. 2(a) (black solid line) may be traced back to the incompleteness of the basis. Neglecting the contribution of the remote modes results in severe violation of current conservation (black dotted line). Since the self-energies are additive, one can separate their contribution to the total current (this is an approximation, of course, because Green's functions determine self-energies and vice versa) [62]. The radiative generation spectrum in Fig. 2(b) shows the photogeneration of carriers in the superlattice absorber, and, unexpectedly, free-carrier absorption in the valence band of the electron barrier. The generation current obtained from the integration of the local generation rate [63] (solid line) is equal to the total current in Fig. 2(a), as expected in the case of complete carrier extraction. A comprehensive simulation of type-II SLs requires the inclusion of defect-mediated nonradiative recombination processes, which determine the extraction efficiency. Recently, a conserving SRH self-energy model fully compatible with the rigorous treatment of electron-photon and electron-phonon scattering within the NEGF formalism was proposed by Aeberhard [64]. In Fig. 2(c) we show the spectral scattering current (color maps) associated to the coupling with polar optical phonons. The phonon-assisted cascade of the (minority) electrons from the conduction miniband of the superlattice absorber across the graded superlattice (relaxation region) is clearly visible.

Encoding the contribution of the remote modes in the self-energy (25) improves significantly the convergence with respect to conventional projection-based approaches. Because of memory limitations of our parallel OpenMP implementation, a convergence analysis with respect to the partition of the modes in near and remote sets is practicable only for the InAs/GaSb absorber; see Fig. 3. Convergence is better assessed on current densities, which are more sensitive to model-order reduction than other single-particle properties such as carrier densities. The speedup in computation time is close to $(n_n/n_t)^3$, as Eq. (25) is evaluated only once at the beginning of the self-consistent cycle (a computational complexity analysis of mode-space approaches is presented in Ref. [44]).

B. Connection to semiclassical approaches and experiments: LWIR T2SLs

We now turn our attention to the interpretation of the NEGF results from a semiclassical perspective. As a genuine quantum transport model, NEGF provides a

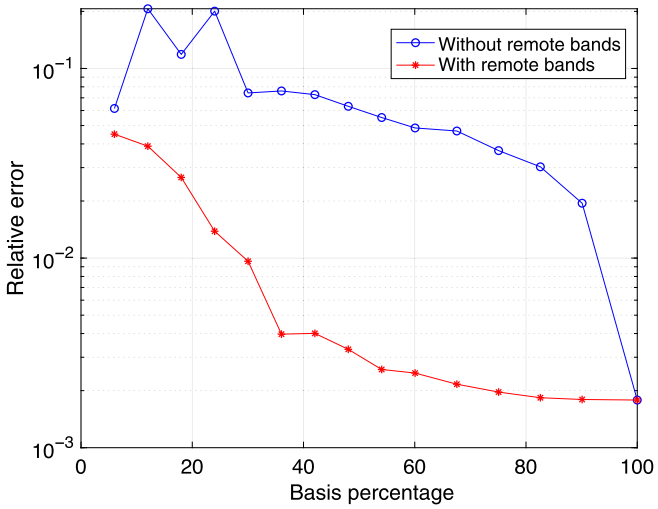

FIG. 3. Standard deviation of the photocurrent fluctuations normalized with respect to the mean spatial average, as a function of n_n/n_t, with and without the contribution of the remote modes.

comprehensive tool for the analysis of type-II SL photodetectors, with transport and generation-recombination processes encoded in energy- and momentum-dependent scattering self-energies. Nevertheless, it is interesting and useful to explore the connection between NEGF models and semiclassical approaches successfully applied to bulk MCT devices. Macroscopic quantities such as carrier mobilities and lifetimes are admittedly not germane to the NEGF formalism, but they represent critical ingredients needed in quantum-corrected drift-diffusion (DD) models [65]. A notable example is landscape localization theory, in which coherent processes such as localization and tunneling effects are included by means of an effective potential derived from a (nonautonomous) Schroedinger-like equation, while dissipative processes have to be described by appropriate mobilities [66,67]. A mobility study could also be the starting point to develop fractional DD approaches, which may offer a unified description of carrier transport in disordered SLs, accounting for memory effects associated to trapping mechanisms, along the lines of recent investigations on anomalous (non-Fickian) transport in disordered organic semiconductors [68].

Different techniques were proposed to extract the mobility from quantum transport simulations. A dispersive, time-dependent diffusion coefficient was obtained from Monte Carlo simulations of AlAs/GaAs disordered SLs [69]. An "apparent" position-dependent mobility was proposed in a study of diffusive transport in fully depleted silicon-on-insulator transistors, bridging the gap between a Scharfetter-Gummel DD and NEGF models [70]. An efficient method to extract an effective mobility from NEGF and Kubo-Greenwood calculations, while minimizing contact resistance contamination and channel length misestimates, was discussed in the context of thin silicon films [71]. In the context of type-II SLs, electron and hole mobilities may be computed from $v_{n,p} = \mu_{n,p} F$, where F is the electric field and $v_{n,p}$ are the carrier velocities

$$v_{n,p} = \left\langle \frac{J_{n,p}}{\rho_{n,p}} \right\rangle \tag{26}$$

obtained from the NEGF carrier densities $\rho_{n,p}$ and current densities $J_{n,p}$.

The electronic structure computed with periodic boundary conditions [26] is shown in Fig. 4. The cutoff wavelength is found to be 11.8 μm, close to the experimental value of 12.5 μm extracted from low-temperature photoluminescence spectra [59]. The local density of states shown in Fig. 5 reveals that the conduction minibands width Δ is larger than the gaps between them, while for the highest valence miniband, Δ is smaller than 1 meV (this value is obtained directly from the dispersion of the band structure along k_z, and so it does not include homogeneous or inhomogeneous broadening). The difference in Δ, which in part is due to the relatively low conduction band offsets in InAs/(In, As)Sb SLs, has a profound effect on the electron and hole transport properties. Although the spatially resolved spectral current in both n- and p-type SLs looks similar for small electric fields (see the continuous stripes crossing the band diagrams in Fig. 5), the nature of carrier

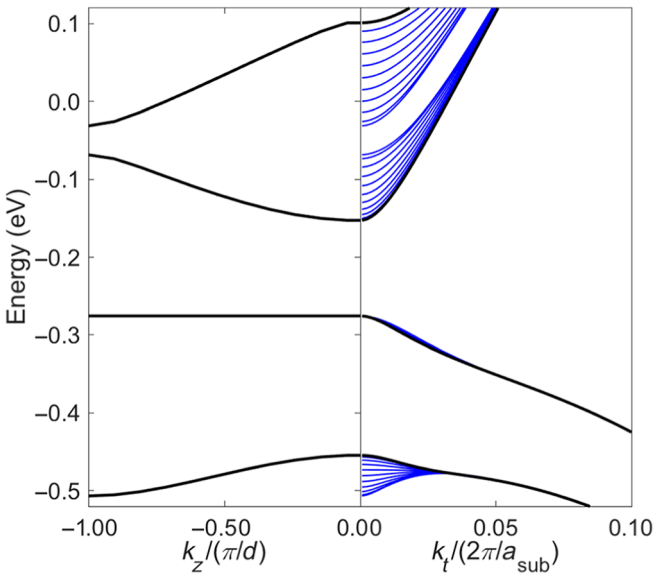

FIG. 4. The $k \cdot p$ subband structure of the SL considered in Ref. [59], consisting in the alternating sequence of 10.26 nm $InAs_{0.97}Sb_{0.03}$ and 1.89 nm $InAs_{0.55}Sb_{0.45}$, plotted versus wavevectors along the in-plane (left panel) and growth directions (right panel). The in-plane dispersion for $k_z = 0$ is shown in black, while the blue curves are for equally spaced values of k_z up to the mini-Brillouin-zone boundary π/d (d is the SL period). Bowing parameters of the Luttinger parameters are computed as in Ref. [23].

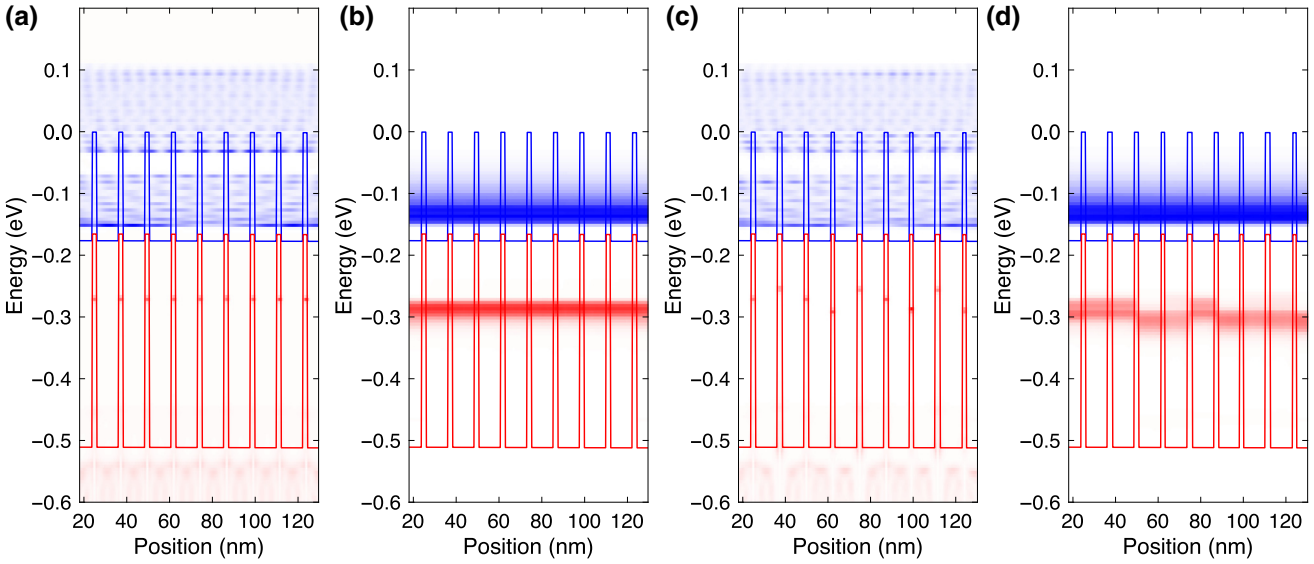

FIG. 5. Local density of states shown for $\underline{k} = 0$, computed for the ordered (a) and disordered SL (c). The applied electric field is $F = 0.1$ kV/cm. The first valence miniband (the sharp red peaks in the LDOS) is strongly localized in both energy and space; energy alignments are severely disrupted by the disorder, while the wider conduction minibands are not visibly affected, suggesting that hole transport is likely to be more sensitive to disorder. This is confirmed by the spatially resolved current spectrum shown in the ordered (b) and disordered (d) structure. The energy-integrated current drops by approximately one order of magnitude in the presence of geometrical fluctuations at $T = 200$ K.

transport for electrons and holes is very different. A closer inspection of the current components reveals that electron transport is mainly a coherent process through extended Bloch states at low fields, which can be expressed by the familiar Landauer-Büttiker formula

$$I_{\text{coherent}} = \frac{e}{\hbar}\,\text{Tr}\{\Gamma_1^B G^R \Gamma_2^B G^A\}(f_1 - f_2), \qquad (27)$$

where the $\Gamma_{1,2}^B$ are the broadening functions of the two contacts. On the other hand, hole transport is entirely noncoherent even in the low-field limit, meaning that the holes, strongly localized in the weakly coupled (In, As)Sb quantum wells, can move across the miniband only if assisted by scattering mechanisms such as carrier-phonon interactions (I_{coherent} is negligible compared to the scattering current).

In Fig. 6 we show the electron and hole drift velocities as a function of the electric field at $T = 200$ K. The velocities are almost linear for low fields, confirming that the structure is long enough to reach the ohmic drift velocity regime. The critical field at which the electron drift velocity peaks is approximately 4 kV/cm, which corresponds to a potential drop per period $eFd = 5$ meV. From a semiclassical perspective, beyond this critical field, the electrons experience unscattered Bloch oscillations in the mini-Brillouin zone, which do not contribute to the net current. For higher fields, the Bloch oscillations should eventually lead to the breaking of the miniband into a ladder of Wannier-Stark (WS) levels, and carrier transport is best described by hopping between the states of the WS ladder rather than by miniband transport. However, due to the large width of the electron minibands and their relative small separation in energy, this condition is never reached. For higher fields, the electron velocity increases again because coherent tunneling between minibands (interminiband transport) becomes possible.

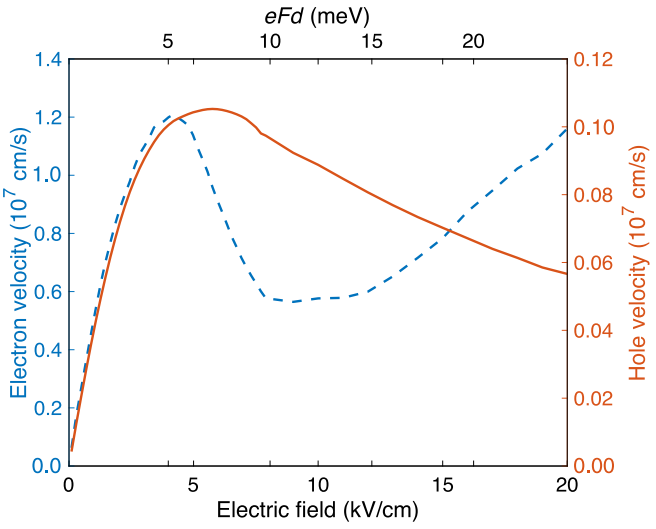

FIG. 6. Electron (left axis, dashed blue curve) and hole (right axis, solid red curve) velocities as a function of the applied electric field (lower axis) and of the potential drop per period eFd (upper axis), at $T = 200$ K.

In *n*-type LWIR T2SLs, a low hole velocity and therefore a low collection efficiency is expected from the large band-edge hole effective mass in the growth direction, and perhaps for this reason, most LWIR detectors have been based on *p*-type absorbers; the experimental evidence that hole mobility in T2SLs is not as poor as expected was explained with the anisotropy and nonparabolicity of the valence band away from the band edge [56]. Our calculations indicate that the hole velocity, although approximately one order of magnitude smaller than the electron velocity, is significantly higher than expected. Esaki-Tsu theory [72] of superlattice transport in terms of Bloch oscillations fails for such a narrow miniband, as $eFd \gg \Delta$ for any realistic field F. Hole transport is always dissipative. The spectral scattering rates indicate that near the flatband condition, the holes move across the superlattice by hopping up and down the miniband, emitting and absorbing polar optical phonons. At higher fields, a WS ladder is clearly visible and electron hopping in the valence band is mostly a downhill process governed by the spontaneous emission of phonons [73].

The velocity-field curves in Fig. 6 are computed for an ideal SL, but the very concept of miniband becomes questionable when Δ becomes very small, due to crystal imperfections and other departures from ideality. Experimental investigations of vertical hole transport in type-II antimonide-based SLs provide a clear indication of the presence of hopping mechanisms between trap states, with hole transport characteristics similar to those seen in amorphous semiconductors displaying Anderson localization. Olson *et al.* estimated the hole mobility by measuring minority carrier lifetimes and the fraction of injected holes that diffuse in the T2SL base region of a bipolar transistor; different slopes in the Arrhenius plot of the hole mobility were attributed by the authors to distinct transport regimes, from miniband transport of thermally activated carriers, to a regime dominated by hopping within defect states above the miniband mobility edge [59]. In a SL, the disorder may originate from crystal defects, interface roughness, and compositional and thickness fluctuations of the layers. In order to investigate carrier transport in disordered SLs, we randomly add or subtract one ML to each layer, breaking the translational symmetry along the growth axis. The effect of the disorder is particularly evident for the hole miniband, which appears to be severely disrupted; see the local density of states shown in Fig. 5(c) and the spectral current densities in Fig. 5(d). And, in fact, the hole current at $T = 200$ K is reduced by one order of magnitude with respect to the ordered structure, while the electron current is nearly unaffected at the same temperature.

In Fig. 7 we show the electron and hole low-field mobilities (at $F = 0.1$ kV/cm) of the disordered SL as a function of inverse temperature. The electron mobility μ_n shows the conventional phonon-limited temperature dependence above 80 K, in which carrier-phonon scattering slows down the electron velocity, which is typical of miniband conduction. At lower temperatures, the energy-resolved current density becomes spectrally narrower, involving mainly the less extended states near the bottom of the conduction miniband, which results in a slight decrease of μ_n. On the other hand, the hole mobility is thermally activated in the whole temperature range. The calculated hole mobilities are smaller than the experimental results obtained by Olson, especially at higher temperatures, probably because the disorder is applied to the whole SL, irrespectively of the lateral degree of freedom. In general, in a SL sample of macroscopic size, the well and barrier thicknesses may fluctuate in the layer plane, meaning that fully localized states along the growth axis may coexist with miniband states sufficiently extended to allow transport, so that percolative transport along high conduction paths may even conceal the presence of localized states from mobility experiments. The activation energy estimated from our calculations $E_a = 17.1$ meV is very close to that reported in Ref. [59] for region 3 ($E_a = 16$ meV), in which transport was considered to be dominated by hopping between localized states near the mobility edge, in the exponential tail of the valence miniband.

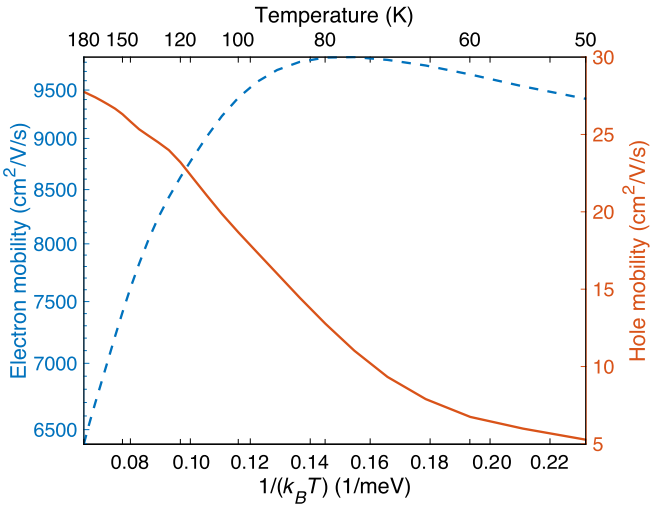

FIG. 7. Electron (left axis, dashed blue curve) and hole (right axis, solid red curve) mobilities of the disordered SL as a function of inverse temperature, computed for an electric field of 0.1 kV/cm.

IV. CONCLUSION

Scaled on cluster architectures, the mode-space approach, corrected to include the effect of the remote bands, is an enabling tool towards the simulation of realistic T2SL photodetectors. While it is difficult to combine the two pictures at opposite ends of the possible transport mechanisms—miniband transport and hopping regime—in a semiclassical theory that is valid at all fields and temperatures, the NEGF approach seamlessly describes situations

in which the main ingredients, e.g., miniband widths, localization effects due to electric fields, geometrical and compositional fluctuations, and scattering-induced broadening, determine a smooth transition between transport regimes. This is the most probable scenario in the realm of IR SL detectors.

ACKNOWLEDGMENTS

We thank Urs Aeberhard and Jonathan Schuster for useful discussions. This work was supported by the U.S. Army Research Laboratory through the Collaborative Research Alliance (CRA) for MultiScale multidisciplinary Modeling of Electronic materials (MSME). The computational resources were provided by HPC@POLITO [74], the DoD HPC Systems, and the 2019 Army Research Office DURIP Award (Grant No. W911NF-19-1-0161) made to Dr. E. Bellotti.

[1] A. Rogalski, P. Martyniuk, and M. Kopytko, InAs/GaSb type-II superlattice infrared detectors: Future prospect, Appl. Phys. Rev. **4**, 031304 (2017).
[2] S. Steiger, Ph.D. thesis, Eidgenössische Technische Hochschule Zürich, 2009.
[3] U. Aeberhard, Ph.D. thesis, Eidgenössische Technische Hochschule Zürich, 2008.
[4] U. Aeberhard, Photovoltaics at the mesoscale: Insights from quantum-kinetic simulation, J. Phys. D **51**, 323002 (2018).
[5] A small imaginary potential $i\eta$ is included in the Keldysh components of the self-energy. While these terms are negligible in the interacting case, they are needed to start the self-consistent Born loop in the presence of bound states lying outside the bandwidth of the contacts [75]. After the first iteration, η is set to zero to ensure current conservation.
[6] Y. Wei and M. Razeghi, Modeling of type-II InAs/GaSb superlattices using an empirical tight-binding method and interface engineering, Phys. Rev. B **69**, 085316 (2004).
[7] R. Magri and A. Zunger, Effects of interfacial atomic segregation and intermixing on the electronic properties of InAs/GaSb superlattices, Phys. Rev. B **65**, 165302 (2002).
[8] P. C. Klipstein, Operator ordering and interface-band mixing in the Kane-like Hamiltonian of lattice-matched semiconductor superlattices with abrupt interfaces, Phys. Rev. B **81**, 235314 (2010).
[9] Y. Livneh, P. C. Klipstein, O. Klin, N. Snapi, S. Grossman, A. Glozman, and E. Weiss, $k \cdot p$ model for the energy dispersions and absorption spectra of InAs/GaSb type-II superlattices, Phys. Rev. B **86**, 235311 (2012).
[10] Y. Livneh, P. C. Klipstein, O. Klin, N. Snapi, S. Grossman, A. Glozman, and E. Weiss, Erratum: $k \cdot p$ model for the energy dispersions and absorption spectra of InAs/GaSb type-II superlattices, Phys. Rev. B **90**, 039903(E) (2014).
[11] U. Aeberhard, Challenges in the NEGF simulation of quantum-well photovoltaics posed by non-locality and localization, Phys. Status Solidi B **99**, 1800500 (2019).
[12] M. Luisier, A. Schenk, and W. Fichtner, Quantum transport in two- and three-dimensional nanoscale transistors: Coupled mode effects in the nonequilibrium Green's function formalism, J. Appl. Phys. **100**, 043713 (2006).
[13] D. A. Lemus, J. Charles, and T. Kubis, Mode-space-compatible inelastic scattering in atomistic nonequilibrium Green's function implementations, https://arxiv.org/abs/2003.09536.
[14] D. Z. Ting, A. Soibel, A. Khoshakhlagh, L. Höglund, S. A. Keo, S. B. Rafol, C. J. Hill, A. M. Fisher, E. M. Luong, J. Nguyen, J. K. Liu, J. M. Mumolo, B. J. Pepper, and S. D. Gunapala, in *Proceedings of the SPIE Defense+Security, Infrared Technology and Applications XLIII* (Anaheim, CA, 2017), Vol. 10177, p. 101770N.
[15] D. O. Winge, M. Franckié, C. Verdozzi, A. Wacker, and M. F. Pereira, Simple electron-electron scattering in nonequilibrium Green's function simulations, J. Phys. Conf. Ser. **696**, 012013 (2016).
[16] U. Aeberhard, Quantum transport simulation of hot carrier photocurrent generation in quantum well solar cells, Semiconductor Sci. Technol. **34**, 094002 (2019).
[17] O. Bonno, J.-L. Thobel, and F. Dessenne, Modeling of electron-electron scattering in Monte Carlo simulation of quantum cascade lasers, J. Appl. Phys. **97**, 043702 (2005).
[18] L. C. Hirst, R. J. Walters, M. F. Führer, and N. J. Ekins-Daukes, Experimental demonstration of hot-carrier photocurrent in an InGaAs quantum well solar cell, Appl. Phys. Lett. **104**, 231115 (2014).
[19] S. B. Campana, *The Infrared & Electro-Optical Systems Handbook* (SPIE, Washington, 1993), Vol. 5.
[20] P. Enders, A. Bärwolff, M. Woerner, and D. Suisky, $k \cdot p$ theory of energy bands, wave functions, and optical selection rules in strained tetrahedral semiconductors, Phys. Rev. B **51**, 16695 (1995).
[21] R. G. Veprek, S. Steiger, and B. Witzigmann, Ellipticity and the spurious solution problem of $k \cdot p$ envelope equations, Phys. Rev. B **76**, 165320 (2007).
[22] X. Zhou, F. Bertazzi, M. Goano, G. Ghione, and E. Bellotti, Deriving $k \cdot p$ parameters from full-Brillouin-zone descriptions: A finite-element envelope function model for quantum-confined wurtzite nanostructures, J. Appl. Phys. **116**, 033709 (2014).
[23] P. C. Klipstein, Y. Livneh, A. Glozman, S. Grossman, O. Klin, N. Snapi, and E. Weiss, Modeling InAs/GaSb and InAs/InAsSb superlattice infrared detectors, J. Electron. Mater. **43**, 2984 (2014).
[24] D. Lackner, M. Steger, M. L. W. Thewalt, O. J. Pitts, Y. T. Cherng, S. P. Watkins, E. Plis, and S. Krishna, InAs/InAsSb strain balanced superlattices for optical detectors: Material properties and energy band simulations, J. Appl. Phys. **111**, 034507 (2012).
[25] B. Witzigmann, R. G. Veprek, S. Steiger, and J. Kupec, Comprehensive modeling of optoelectronic nanostructures, J. Comp. Electron. **8**, 389 (2009).
[26] P.-F. Qiao, S. Mou, and S. L. Chuang, Electronic band structures and optical properties of type-II superlattice photodetectors with interfacial effect, Opt. Express **20**, 2319 (2012).
[27] G. Liu and S.-L. Chuang, Modeling of Sb-based type-II quantum cascade lasers, Phys. Rev. B **65**, 165220 (2002).

[28] R. G. Veprek, Ph.D. thesis, Eidgenössische Technische Hochschule Zürich, 2009.
[29] F. Bertazzi, M. Goano, G. Ghione, A. Tibaldi, P. Debernardi, and E. Bellotti, in *Handbook of Optoelectronic Device Modeling and Simulation*, edited by J. Piprek (CRC Press, Boca Raton, FL, 2017), Chap. 2, p. 35.
[30] M. Luisier, A. Schenk, W. Fichtner, and G. Klimeck, Atomistic simulation of nanowires in the $sp^3d^5s^*$ tight-binding formalism: From boundary conditions to strain calculations, Phys. Rev. B **74**, 205323 (2006).
[31] A. Fasolino, E. Molinari, and J. C. Maan, Calculated superlattice and interface phonons of InAs/GaSb superlattices, Phys. Rev. B **33**, 8889(R) (1986).
[32] H. Liu, N. Yue, Y. Zhang, P. Qiao, D. Zuo, B. Kesler, S. L. Chuang, J.-H. Ryou, J. D. Justice, and R. Dupuis, Lattice vibration modes in type-II superlattice InAs/GaSb with no-common-atom interface and overlapping vibration spectra, Phys. Rev. B **91**, 235317 (2015).
[33] H. Liu, Y. Zhang, E. H. Steenbergen, S. Liu, Z. Lin, Y.-H. Zhang, J. Kim, M.-H. Ji, T. Detchprohm, R. D. Dupuis, J. K. Kim, S. D. Hawkins, and J. F. Klem, Raman scattering study of lattice vibrations in the type-II superlattice InAs/$InAs_{1-x}sb_x$, Phys. Rev. Appl. **8**, 034028 (2017).
[34] B. K. Ridley, ed., *Electrons and Phonons in Semiconductor Multilayers*, Cambridge Studies in Semiconductor Physics and Microelectronic Engineering (Cambridge University Press, Cambridge, UK, 1996).
[35] M. R. Wood, Ph.D. thesis, Texas A&M University, 2017.
[36] F. Compagnone, M. Manenti, A. Di Carlo, and P. Lugli, Hot electrons and hot phonons in quantum cascade lasers, Physica B **314**, 336 (2002).
[37] U. Aeberhard and R. H. Morf, Microscopic nonequilibrium theory of quantum well solar cells, Phys. Rev. B **77**, 125343 (2008).
[38] K. Hess, ed., *Monte Carlo Device Simulation: Full Band and Beyond* (Kluwer Academic, Boston, 1991).
[39] "Ioffe Physico-Technical Institute, St. Petersburg, Russia, "Physical properties of semiconductors",".
[40] L. E. Henrickson, Nonequilibrium photocurrent modeling in resonant tunneling photodetectors, J. Appl. Phys. **91**, 6273 (2002).
[41] A. Buin, A. Verma, and S. Saini, Optoelectronic response calculations in the framework of $k \cdot p$ coupled to non-equilibrium Green's functions for one-dimensional systems in the ballistic limit, J. Appl. Phys. **114**, 033111 (2013).
[42] L. C. Lew Yan Voon and L. R. Ram-Mohan, Tight-binding representation of the optical matrix elements: Theory and applications, Phys. Rev. B **47**, 15500 (1993).
[43] S. Datta, *Electronic Transport in Mesoscopic Systems* (Cambridge University Press, Cambridge, UK, 1995).
[44] L. Zeng, Y. He, M. Povolotskyi, X. Liu, G. Klimeck, and T. Kubis, Low rank approximation method for efficient Green's function calculation of dissipative quantum transport, J. Appl. Phys. **113**, 213707 (2013).
[45] S.-C. Lee and A. Wacker, Nonequilibrium Green's function theory for transport and gain properties of quantum cascade structures, Phys. Rev. B **66**, 245314 (2002).
[46] A. Wacker, M. Lindskog, and D. O. Winge, Nonequilibrium Green's function model for simulation of quantum cascade laser devices under operating conditions, IEEE J. Select. Topics Quantum Electron. **19**, 1200611 (2013).
[47] Y. Lee, D. Logoteta, N. Cavassilas, M. Lannoo, M. Luisier, and M. Bescond, Quantum treatment of inelastic interactions for the modeling of nanowire field-effect transistors, Materials **13**, 60 (2019).
[48] M. Bescond, C. Li, H. Mera, N. Cavassilas, and M. Lannoo, Modeling of phonon scattering in *n*-type nanowire transistors using one-shot analytic continuation technique, J. Appl. Phys. **114**, 153712 (2013).
[49] H. Mera, M. Lannoo, N. Cavassilas, and M. Bescond, Nanoscale device modeling using a conserving analytic continuation technique, Phys. Rev. B **88**, 075147 (2013).
[50] H. Mera, T. G. Pedersen, and B. K. Nikolic, Hypergeometric resummation of self-consistent sunset diagrams for steady-state electron-boson quantum many-body systems out of equilibrium, Phys. Rev. B **94**, 165429 (2016).
[51] Y. Lee, M. Lannoo, N. Cavassilas, M. Luisier, and M. Bescond, Efficient quantum modeling of inelastic interactions in nanodevices, Phys. Rev. B **93**, 205411 (2016).
[52] Y. Lee, M. Bescond, N. Cavassilas, D. Logoteta, L. Raymond, M. Lannoo, and M. Luisier, Quantum treatment of phonon scattering for modeling of three-dimensional atomistic transport, Phys. Rev. B **95**, 201412(R) (2017).
[53] U. Aeberhard, Theory and simulation of quantum photovoltaic devices based on the non-equilibrium Green's function formalism, IEEE J. Quantum Electron. **10**, 394 (2011).
[54] W. Lee, N. Jean, and S. Sanvito, Exploring the limits of the self-consistent born approximation for inelastic electronic transport, Phys. Rev. B **79**, 085120 (2009).
[55] S. M. Komirenko, K. W. Kim, M. A. Stroscio, and M. Dutta, Applicability of the Fermi golden rule and the possibility of low-field runaway transport in nitrides, J. Phys. Condens. Matter **13**, 6233 (2001).
[56] D. Z. Ting, A. Soibel, and S. D. Gunapala, Hole effective masses and subband splitting in type-II superlattice infrared detectors, Appl. Phys. Lett. **108**, 183504 (2016).
[57] J. Schuster, Assessment of the modulation transfer function in infrared detectors with anisotropic material properties: Type-II superlattices, IEEE Trans. Electron. Devices **66**, 1338 (2019).
[58] Z. Tian, R. T. Hinkey, R. Q. Yang, D. Lubyshev, Y. Qiu, J. M. Fastenau, W. K. Liu, and M. B. Johnson, Interband cascade infrared photodetectors with enhanced electron barriers and *p*-type superlattice absorbers, J. Appl. Phys. **111**, 024510 (2012).
[59] B. V. Olson, J. F. Klem, E. A. Kadlec, J. K. Kim, M. D. Goldflam, S. D. Hawkins, A. Tauke-Pedretti, W. T. Coon, T. R. Fortune, E. A. Shaner, and M. E. Flatté, Vertical Hole Transport and Carrier Localization in InAs/$InAs_{1-x}Sb_x$ Type-II Superlattice Heterojunction Bipolar Transistors, Phys. Rev. Appl. **7**, 024016 (2017).
[60] Operating under zero bias, ICIPs create one electron from a number of photons equal to the number of the constituent stages, which is exactly the opposite of quantum cascade lasers, and the photosignal is determined by the stage with

the smallest photocurrent, usually the last one from the illuminated contact.

[61] A charge self-consistent electronic-structure model for type-II broken-gap superlattices based on a multiband $k \cdot p$ envelope-function framework was proposed in Ref. [76] to avoid the ambiguous classification of electron and hole states when conduction and valence bands strongly intermix.

[62] T. Schmielau, M. F. Pereira, Jr., Nonequilibrium many body theory for quantum transport in terahertz quantum cascade lasers, Appl. Phys. Lett. **95**, 231111 (2009).

[63] U. Aeberhard, Photocarrier extraction in GaAsSb/GaAsN type-II QW superlattice solar cells, Appl. Phys. Lett. **112**, 213904 (2018).

[64] U. Aeberhard, Nonequilibrium Green's function picture of nonradiative recombination of the Shockley-Read-Hall type, Phys. Rev. B **99**, 125302 (2019).

[65] A. Tibaldi, F. Bertazzi, M. Goano, R. Michalzik, and P. Debernardi, VENUS: A vertical-cavity surface-emitting laser electro-opto-thermal numerical simulator, IEEE J. Select. Topics Quantum Electron. **25**, 1500212 (2019).

[66] M. Filoche, M. Piccardo, Y.-R. Wu, C.-K. Li, C. Weisbuch, and S. Mayboroda, Localization landscape theory of disorder in semiconductors. I. Theory and modeling, Phys. Rev. B **95**, 144204 (2017).

[67] T.-Y. Tsai, K. Michalczewski, P. Martyniuk, C.-H. Wu, and Y.-R. Wu, Application of localization landscape theory and the $k \cdot p$ model for direct modeling of carrier transport in a type II superlattice InAs/InAsSb photoconductor system, J. Appl. Phys. **127**, 033104 (2020).

[68] K. Y. Choo, S. V. Muniandy, K. L. Woon, M. T. Gan, and D. S. Ong, Modeling anomalous charge carrier transport in disordered organic semiconductors using the fractional drift-diffusion equation, Org. Electron. **41**, 157 (2017).

[69] L.-W. Wang and A. Zunger, Pseudopotential-based multiband $k \cdot p$ method for $\sim 250\,000$-atom nanostructure systems, Phys. Rev. B **54**, 11417 (1996).

[70] G. Mugny, F. G. Pereira, D. Rideau, F. Triozon, Y. M. Niquet, M. Pala, D. Garetto, and C. Delerue, in *ESSDERC 2016. Proceedings of the 46th European Solid State Device Research Conference (Lausanne)* (IEEE, 2016), p. 424.

[71] Y.-M. Niquet, V.-H. Nguyen, F. Triozon, I. Duchemin, O. Nier, and D. Rideau, Quantum calculations of the carrier mobility: Methodology, Matthiessen's rule, and comparison with semi-classical approaches, J. Appl. Phys. **115**, 054512 (2014).

[72] S. Rott, P. Binder, N. Linder, and G. H. Döhler, A combined model for miniband and hopping transport in superlattices, Physica E **2**, 511 (1998).

[73] Monte-Carlo calculations of hopping transport predict a weak temperature dependence of the drift velocity in these conditions, since phonon absorption and stimulated emission, whose rates increase with temperature, tend to cancel each other, and the only contribution to the current is therefore the spontaneous emissions of phonons [72].

[74] See http://www.hpc.polito.it.

[75] K. S. Thygesen and A. Rubio, Conserving GW scheme for nonequilibrium quantum transport in molecular contacts, Phys. Rev. B **77**, 115333 (2008).

[76] T. Andlauer and P. Vogl, Full-band envelope-function approach for type-II broken-gap superlattices, Phys. Rev. B **80**, 035304 (2009).